LBL-26144

Lawrence Berkeley Laboratory
UNIVERSITY OF CALIFORNIA

Materials & Chemical Sciences Division

Invited paper for symposium, ASM Congress,
Chicago, IL, September 26–30, 1988

Transmission Electron Microscopy: Imaging of Materials

G. Thomas

October 1988

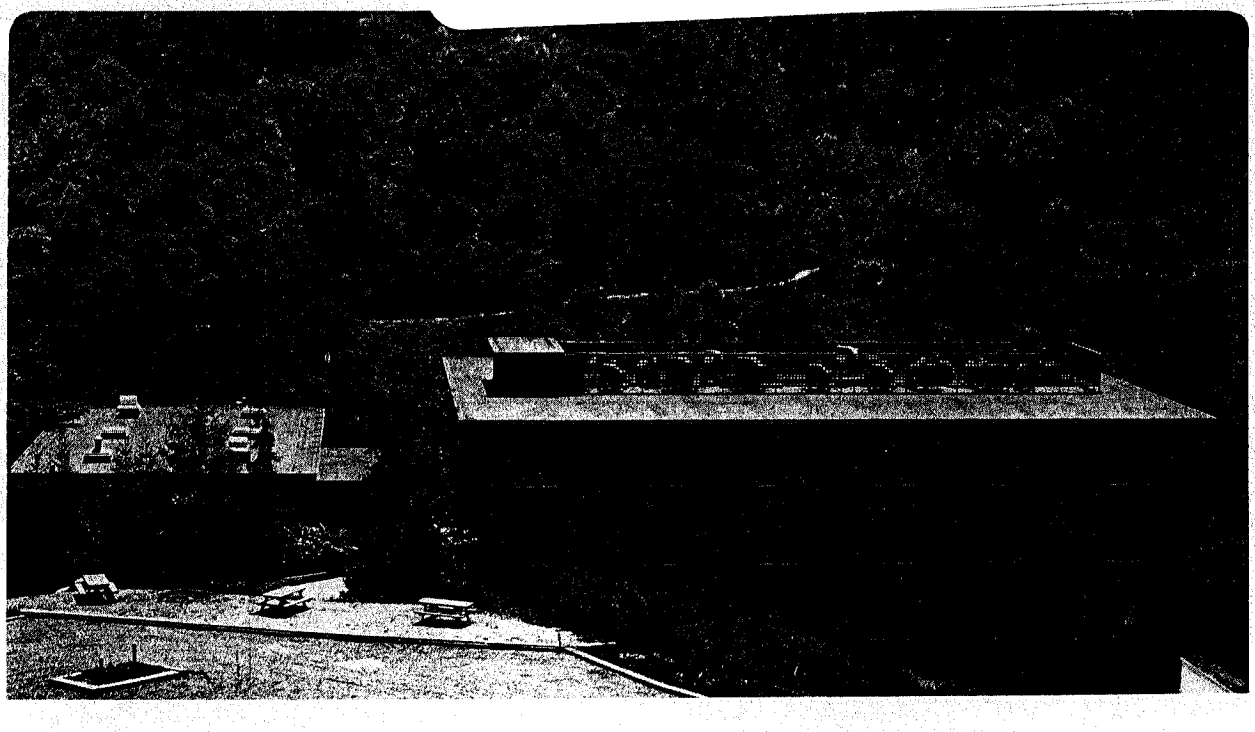

Prepared for the U.S. Department of Energy under Contract Number DE-AC03-76SF00098.

LBL-26144

Transmission Electron Microscopy: Imaging of Materials

Gareth Thomas

Department of Materials Science and Mineral Engineering
University of California
and
Scientific Director
National Center for Electron Microscopy
Materials and Chemical Sciences Division
Lawrence Berkeley Laboratory
1 Cyclotron Road
Berkeley, California 94720
USA

October 1988

TRANSMISSION ELECTRON MICROSCOPY; IMAGING OF MATERIALS

Gareth Thomas, Scientific Director, National Center for Electron Microscopy, MCSD, Lawrence Berkeley Laboratory, Prof.Dept. of Materials Sciences, University of California, Berkeley, CA 94720

1. Introduction: "Metallography" has been a major tool in metallurgy for centuries (fig. 1) and there is no doubt that the development of electron microscopy (1) originating from Ruska and his colleagues in 1932 (fig. 2) and its synergism with materials has lead to dramatic developments in our understanding of structure-property relationships over a wide range of materials (Table 1). Now metallographers can achieve the dream of atomic resolution with the new generation of electron microscopes exemplified by the unique "ARM" installed in Berkeley in 1983 (fig. 3) by which interpretable point to point resolution of 1.6A^{o} is possible over $\pm 40^{o}$ of tilt.

The primary advantage of electron microscopy (TEM), which is truly a diagnostic tool, is of course its very high resolution, and the ability to detect and record the various events that occur when materials are bombarded with electrons, (elastic, inelastic, coherent and incoherent), so that in one instrument it is possible to combine imaging, diffraction and spectroscopy, in-situ, for static and dynamic experiments as shown schematically in (fig. 4). The information so obtained provides great insights into materials behavior and helps enormously to understand and improve materials performance. It is necessary however to examine enough samples in the microscope in order to

arrive at statistically significant conclusions, because the volume of materials per micrograph is very small ($\sim 0.4\mu^3$). The most important problem is still specimen preparation - herein lies the microscopists' art! On a personal note, I have been fortunate to participate in the development of electron microscopy and its applications in metallurgy and materials sciences since I started my graduate studies with Jack Nutting at Cambridge University in 1952. In the following, I have selected representative examples of some of the major imaging methods in TEM which we have applied to various problems in materials. However, I have made no attempt to be comprehensive, but Table 1 summarizes the major developments.

2. Imaging and Interpretation: As is well known, the formation of images in the electron microscope is done by a system of lenses which allow fine probes of electrons to pass through a specimen. These are brought to diffraction focus in the objective back focal plane and transformed to an image by magnifying lenses. Two general methods are used viz., a) amplitude contrast imaging which is not limited by instrument resolution and b) phase contrast-high resolution imaging to be discussed in detail in Gronsky's paper which follows. The basic principles of imaging in bright and dark field, use of multiple images, special effects at high voltage, diffraction, structure imaging, spectroscopy etc, ie., the whole "bag of tools" for expert microscopy are well described e.g., in the references (2-6) given at the end of this paper. Routinely, choice of orientation and imaging conditions is done via the diffraction

pattern and interpretation involves constant interchanges between imaging and diffraction.

3. Examples: The earliest studies of metals were concerned with lattice defects especially dislocations, their origin, motion, multiplication etc. (fig. 5) verifying theories which were already two decades old. But also new defects were discovered, e.g, the tetrahedron (fig. 6). The development of contrast analysis notably the invisibility criterion $\bar{g}.\bar{R}=o$, where $\bar{g}$ is the reciprocal lattice vector and $\bar{R}$ the displacement vector of the defect is illustrated for interfacial dislocations in (fig.7) and compositional faults in TaC (fig. 8). The resolution (i.e, image width) of such defects depends on the material and the effective extinction distance , ξg, which is utilized by weak-beam dark field (fig. 10), or bright field high order imaging (fig. 11). to minimize the wide of the image to achieve kinematical rather than dynamical contrast. In-situ dynamic studies showed many of the predicted properties of lattice defects and climb experiments (fig. 12) lead to useful diffusion data for aluminum alloys. Other defects common to a wide range of materials include accommodation twinning to minimise shape and strain deformation following phase transformations, e.g, (fig. 13), ordered domains (in which APB's can be analysed) as in (fig. 14), enantiomorphic domains in Li ferrite (fig. 15), interstitial ordering (fig. 16) and short range order revealed as domains by lattice imaging (fig. 17). Magnetic domains and boundaries can be imaged by Lorentz microscopy but at low spatial resolution (fig. 18). Much

activity has also been given to studies of alloys. Figure 19 shows how imaging of the diffuse streak due to thin plate G.P. zones in Al-Cu alloys provides a dark field strain free image. The advantages of the TEM are clearly in defining local morphological details such as precipitate-free zones, common in N+G reactions (fig. 20) but not present in spinodals (fig. 21). Figure 22 shows the loss of coherency upon coarsening of a spinodal. In N+G transformations heterogeneous nucleation at defects is common leading to non-uniform structures and, of course, properties. Al alloys are typical examples (figs. 23, 27-30) but the Al-Li base alloys appear to initially undergo spinodal ordering (fig. 24) out of which the δ' phase coarsens (figs. 25, 26). Notice that the morphologies depend on composition, e.g., the faceting in (fig. 26). Another form of heterogeneous precipitation is shown in (fig. 31a) for B+P diffusion in silicon. In the [112] orientation the stresses due to diffusion must be accommodated both by precipitation on $(11\bar{1})$ and dislocation generation of Burgers vectors $a/2\ [1\bar{1}0]$ in the same region. By dark field imaging in a systematic many-beam condition, the specimen can be selectively imaged near the top and bottom surfaces, showing in this [111] orientation that dislocations and precipitates form at different depths after diffusion (fig. 31 b,c).

As emphazied in the introduction, diffraction is a key aspect in imaging. In complex low symmetry materials the use of Kikuchi maps (fig. 32) and convergent beam pattern maps (fig. 33) greatly facilitate control of imaging as well as providing a wide range of

structural information, as described in Williams's paper.

Steels have also been widely studied by TEM and an example which indicates the use of several different techniques coupled with field atom imaging and atomic spectroscopy is shown in (fig. 34).

In the last decade or two, electron microscopy of minerals and ceramics has become popular since the Apollo missions and geological analyses of moon dust (fig. 35). Generic problems in ceramics relate to grain boundaries (fig. 36) such as the retention of glassy phases after processing with additives. These phases can be detected by the imaging methods illustrated in (fig. 37). Studies of glass crystallisation are being done to try to avoid such phases (fig. 38). Another application for lattice imaging to pyrolitic graphite showed that it is a random fibrous structure (fig. 39) and not amorphous as was interpreted from x-rays. This again illustrates the power of electron microscopy.

More recently, ceramic materials have become even more prominent since the discovery of superconductivity in complex oxides, such as Y-Ba-Cu-O (fig. 40) and Bi-Sr-Ca-Cu-O in which polytypoids of different Tc values form adjacent to grain boundaries (fig. 41). These may be modifed by Pb additions as seen in (fig. 42). Such polytypoid structures are also commonly seen in sialons (fig. 43) as known from the phase diagrams. Unfortunately, as yet, such diagrams are unknown for most ceramic superconductors. Finally, as an example of very high resolution imaging fig. 44a shows the 38A^{o} polytypoid with the cation columns resolved. Figure 45b shows the same image after processing using the

"Semper" computer program.

Acknowledgements I sincerely thank the over 100 graduates and research colleagues that I have worked with since coming to Berkeley in 1960, without whose talents and challenges this paper would not have been possible. The selection of examples has been more of a problem of what to omit rather than what to include and I trust any omissions will not produce offence.

This work is supported by the Director, Office of Energy Research, Office of Basic Energy Sciences, Materials Sciences Division of the U.S. Department of Energy under Contract No. DE-AC03-76SF00098. Structural ceramics research was supported by the National Science Foundation under Grant DMR-80-23461.

General References

1. Early History of the Electron Microscope, L. Marton, San Francisco Press, Inc. 1968.

2. Electron Microscopy of Thin Crystals, P.B. Hirsch, A. Howie, R.B. Nicholson, D.W. Pashley and M.J. Whelan, Butterworths, London, 1965.

3. Transmission Electron Microscopy of Materials, G. Thomas, and M.J. Goringe, Wiley-Interscience, N.Y. 1979.

4. The Operation of the Transmission Electron Microscope, D. Chescoe and P.J. Goodhew, Oxford University Press, (Royal Microscopical Society), 1984.

5. Practical Elec. Mic. in Mat. Sci., D.B.Williams, Philips Elect. Inst. (1984).

6. Practical Elec. Mic. in Mat. Sci., (Mon 1-5), J.W. Edington, Philips Elect. Inst. (1974-1977)

Fig. 1-1 (no caption)

Fig. 1-2 The 1932 operational microscope built by von Ruska and colleagues, Berlin.

Fig. 1-3 The JEOL 400-1000kV atomic resolution microscope at the NCEM, Berkeley.

Fig.1-4 (no caption)

Fig. 1-5 Dislocation sources and multiplication in Al-5% Mg solid solution.

Fig. 1-6 Tetrahedron of stacking faults in quenched gold. (Courtesy J.A. Silcox)

Fig. 1-7 Two beam contrast analysis showing pure edge dislocation networks b=1/2 <110> at the interface between two fcc phases in Cu-Mn-Al.

Fig. 1-8 Shear faults in $TaC_{0.8}$; the lack of complete invisibility of faults in $0\bar{2}2$ shows there is residual structure factor contrast (composition change).

Fig. 1-9 (no caption)

Fig. 1-10 The g-3g weak beam image showing paired 1/2 <110> slip dislocations in Al-2.4% Li deformed 1% after 4hrs. aging 150°C.

Fig. 1-11 The g, 2g, 3g bright field images in GaAs; the dislocations are not dissociated.

Fig. 1-12 (no caption)

Fig. 1-13 (no caption)

Fig. 1-14 Sketch and table showing contrast analysis in DO_3 ordered $Fe_3(Al,Si)$; the APB vectors must be 1/2 <100>.

Fig. 1-15 Bright field and dark field of Li ferrite in multibeam non systematic diffraction conditions; breakdown of Friedel's Law allows enantiomorphs to be identified in the dark field.

Fig. 1-16 In-situ transformation of Ta to a Ta-O phase by interstitial ordering; the strain produces almost 4 fold relaxation, foil in [001].

Fig. 1-17 Lattice image using $000+g_{superlattice}+2g_{fundamental}$ conditions showing presence of short range order i.e. domains of order (double spaced fringes) in disordered matrix (oblique printing).

Fig. 1-18 (no caption)

Fig. 1-19 Bright field, dark field and SAD; dark field imaging of streak from G.P. zones in [001]. Notice lack of resolution due to overlapping strains in the B.F.

Fig. 1-20 PFZ in Al-Mg-Zn alloy -- typical of early comet aircraft alloys which were intergranularly brittle.

Fig. 1-21 Spinodal Cu-Ni-Fe alloy showing no PFZ at grain boundary.

Fig. 1-22 (no caption)

Fig. 1-23 Al-2.4% Li, aged 5 min. 300°C, δ' phase at subboundaries dark field of 100 superlattice (Li_2 phase).

Fig. 1-24 Lattice image showing spinodal ordering in Al-2.5Li-1Cu-1.5Mg (cf to fig.17).

Fig. 1-25 Coarsened spinodal forming δ' particle in Al-2.5Li-1Cu-0.5Mg.

Fig. 1-26 As fig. 25 but in Al-2.4Li-2Cu; Notice faceting of δ'. The dark region in center of figs. 25-26 is contrast from β' Al_3Zr phase.

Fig. 1-27 Heterogeneous nucleation of θ' in aged Al-4%Cu. The θ' plates have a strain $\vec{R}$ normal to the {100} habit. The habits form only for $\vec{R}\cdot\vec{b}\neq 0$ where $\vec{b}$= burgers vector of the nucleating dislocation, i.e. only 2 habits (max).

Fig. 1-28 Heterogeneous nucleation of the variants of the T_1 phase in Al-2.4Li-2Cu aged 8 hrs. 175°C. As in fig. 27; only 2 out of 4 possible {111} variants can form on dislocations.

Fig. 1-29, 30 Heterogeneous nucleation of S phase in Al-2.5Cu-1.2Mg alloy at order/disordered interface. Habit is {210} only 3 out of 4 variants form (fig.30).

Fig.1-31 (a) Heterogeneous formation of precipitates on $(11\bar{1})$ and dislocations with b= 1/2 110 to relieve strain in Si due to P diffusion; notice spacings of the precipitates (b≈1/3 $[11\bar{1}]$) and dislocations.

(b), (c) Image asymmetry in dark field at S+ and S- allows contrast enhancement preferentially at the top (dislocations) and bottom (precipitates), giving a "pseudo" 3-D effect.

Fig. 1-32 Kikuchi map of H. C. P. lattice c/a=1.588.

Fig.1-33 CBD map for tetragonal zirconia.

Fig 1-34 (no caption)

Fig. 1-35 (no caption)

Fig. 1-36 (no caption)

Fig. 1-37 Imaging conditions to reveal intergranular glassy phases; material silicon nitride sintered with Al_2O_3 and MgO. The lattice imaging in (c) must be done under controlled conditions.

Fig. 1-38 Dendritic crystallization in Y-Si-Al-O-N glass annealed 1100°C.

Fig. 1-39 Lattice imaging of pyrolitic intertwined graphite fibers with basal planes resolved ("Jenkins Nightmare" structure).

Fig. 1-40 Structure image of 1-2-3 Y-Ba-Cu-O superconductor showing intercalation of Cu-O layers (arrowed): (a) digitized image; (b) averaged over 10 multislices; (c) rotation after averaging of (b); (d) multislice calculated image; (e) projection of model; (f) the 3-D representation of the faulted structure.

Fig. 1-41 Polytypoid structure in orthorhombic Bi-Sr-Cu-O superconductor showing polytypoids of c = 25Å, 31Å, and 38Å for which T_c is 10°K , 80°K, and 110°K respectively. The lowest T_c phase is at the grain boundary.

Fig. 1-42 As fig. 41 for sample sintered with PbO - the low T_c phase has been eliminated adjacent to the grain boundaries.

Fig. 1-43 Polytypoids in Mg-Si-Al-O-N due to composition changes near the boundary.

Fig. 1-44 Atomic resolution image of the 38Å polytypoid of Bi-Sr-Ca-Cu-O (2223 phase); (b) shows this image processed using "Semper " software: notice the central Cu-O rows of high contrast.

Outline of developments of TEM in materials science research

Year	Specimens	Applications/ Developments	Instrumentation	Resolution*
1932- First operational transmission electron microscope, Berlin (Ruska, Knoll)				
1938- First commercial TEM, Berlin (Ruska, von Borries)				
1940-1950	Replicas 1. Oxide 2. Carbon 3. Plastic	Surfaces Slip steps Extracted particles Fractography	50 kV instruments Single condenser Little or no theory	~100 Å
1949- Heidenreich published first paper on TEM foils; basic theory outlined				
1950-1960	Many developments in instrumentation, specimen preparation methods, and image contrast and diffraction theory for interpretation of data			
	Thin foil techniques 1. From bulk 2. Deposition	Defects Phase transitions	100 kV instruments Contrast theory developed	~5 Å- 20 Å
1960-1970				
	Metals Non-metals Semiconductors Ceramics Minerals	Dynamic, in-situ studies: Information explosion on substructure of solids Ion thinning Radiation damage Microdiffraction	First HVEM built in Toulouse (1.2 MeV) First 3 MeV HVEM built in Toulouse Accessories for in-situ studies Controlled experiments	3 Å
1970-1980	Structure imaging to ~2 Å interpretable resolution; lattice imaging widely used			
	As above Catalysts	Theories for high resolution interpretation developed Quasicrystals	TEM/ STEM analytical, convergent beam Spectroscopy EDXS, EELS Commercial HVEMs 0.5-1.5 MeV General acceptance	2 Å
1980-1990				
	Virtually all materials	Atomic resolution in close-packed solids Surface imaging Small particles Fast computation facilities for interpretation Simulation	Medium voltage HREM/ AEM (100- 400 eV commercially available) Improved analytical capabilities Parallel detection in EELS Wide-spread applications in UHV microscopes Tunneling microscopes	1.5 Å
1986- Nobel Prize to Ernst von Ruska for tunneling microscope (Binnig and Rohrer)				

* Interpretable point-to-point

XBL 8810-3588

Table I

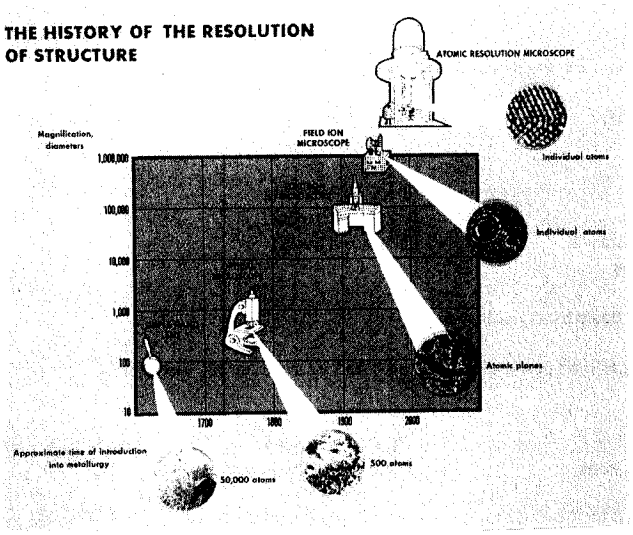

CBB 873-1569

Fig. 1

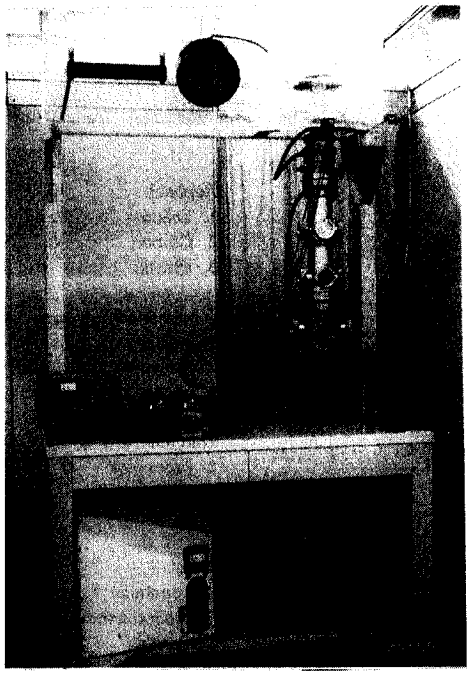

CBB 873-1567

Fig. 2

CHARACTERIZATION BY ELECTRON MICROSCOPY

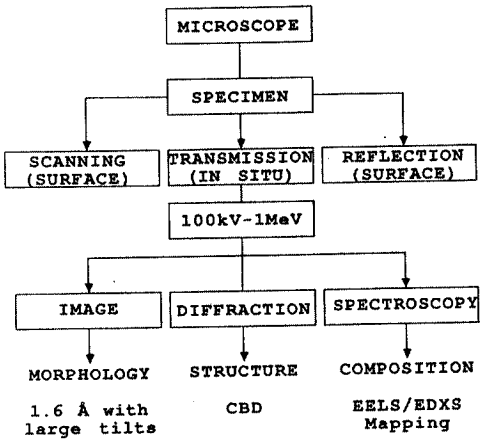

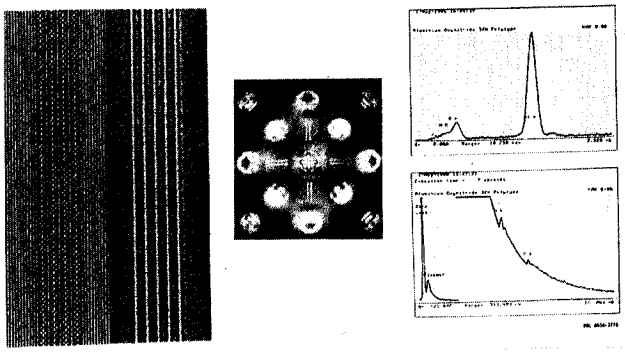

XBB 889-8965

Fig. 4

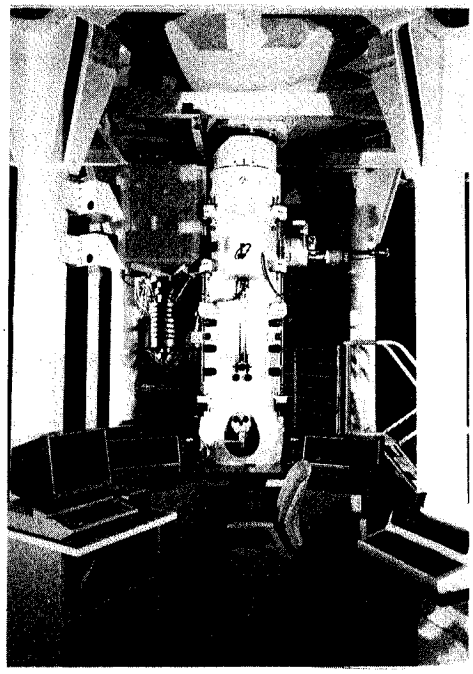

XBB 839-8469

Fig. 3

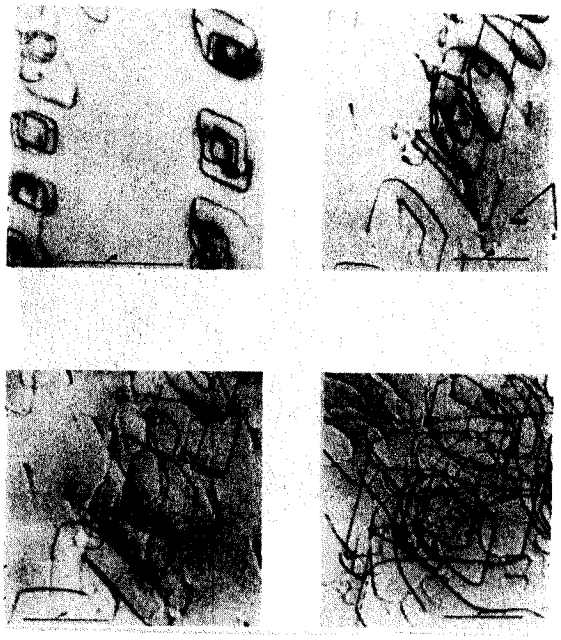

XBB 880-9511

Fig. 5

IM 1734

Fig. 6

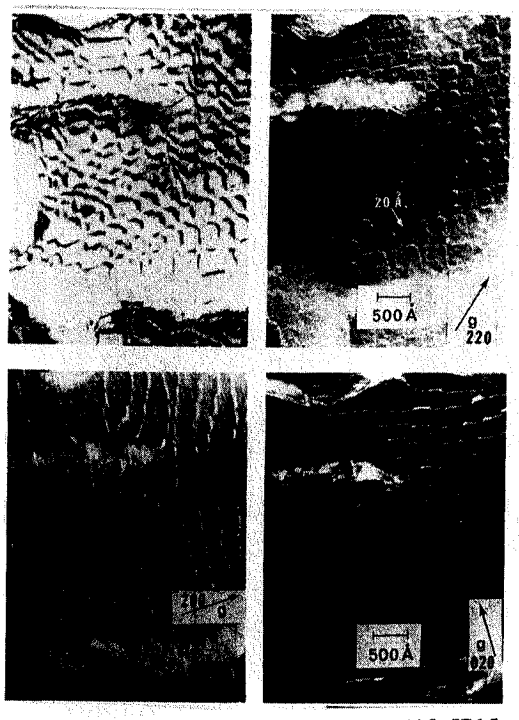

XBB 720-5715

Fig. 7

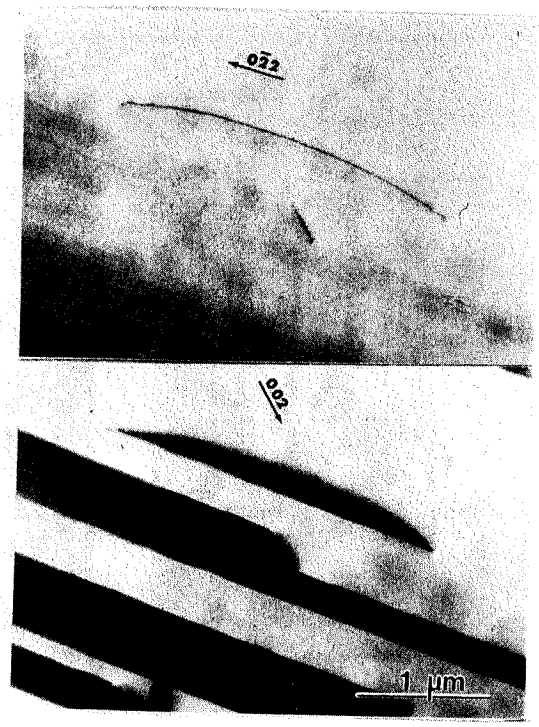

XBB 719-4487

Fig. 8

100 kV	ξ_g			
	Al	Cu	Au	Mg
111	560	242	159	
$1\bar{1}00$				1510

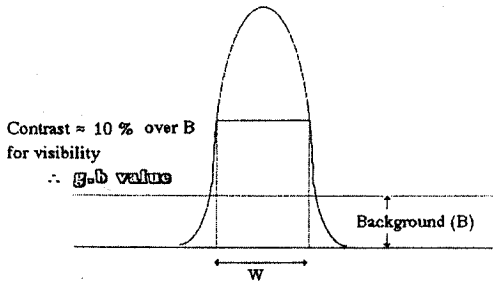

$$w = \frac{\xi_g^{eff}}{3} \quad \text{(many beam } \varepsilon_g\text{)}$$

make ξ_g smaller image is narrower

e.g. increase s >> WBDF
or use ng > 2 HOBF

XBL 8810-3587

Fig. 9

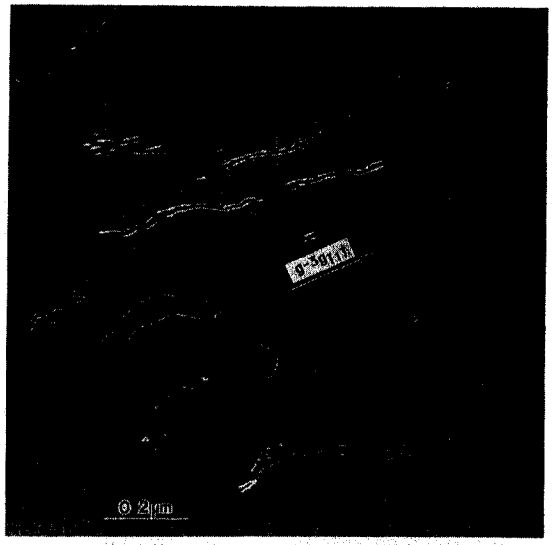

XBB 878-6506

Fig. 10

XBB 713-1046

Fig. 11

Direct observation of the growth of prismatic loops and helicoidal dislocations in an Al-5wt.% Mg alloy during an in-microscope isothermal annealing experiment. Material was quenched from 550°C and aged at room temperature for about 5 years. The isothermal annealing temperature was 130° C. The diffraction conditions were kept nearly constant by employing a Valdre double-tilt hot stage.

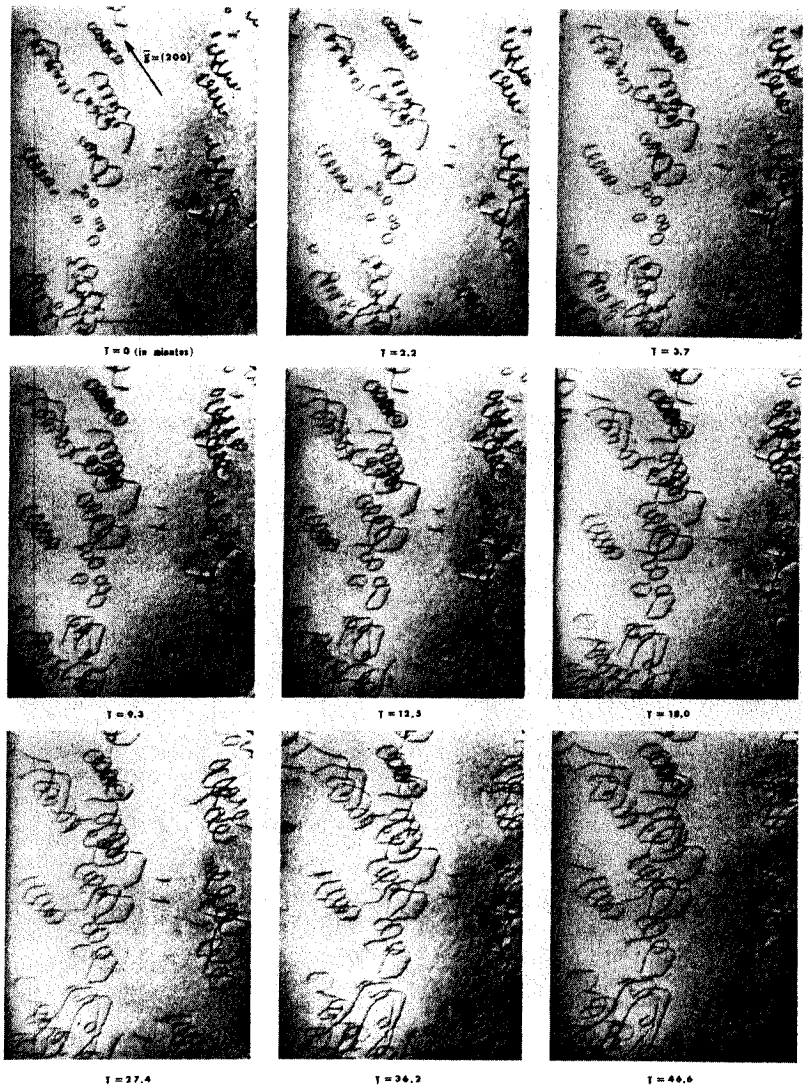

XBB 879-7484

Fig. 12

TWINNING IN MATERIALS

ORTHORHOMBIC InS

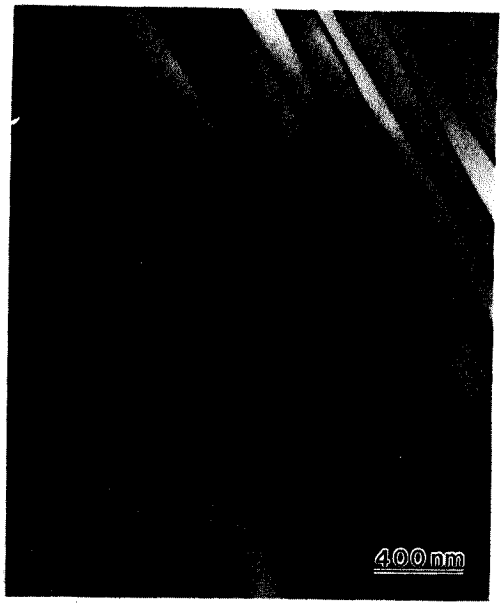

ORTHORHOMBIC $La(Ba,Cu)O_{7-\Delta}$

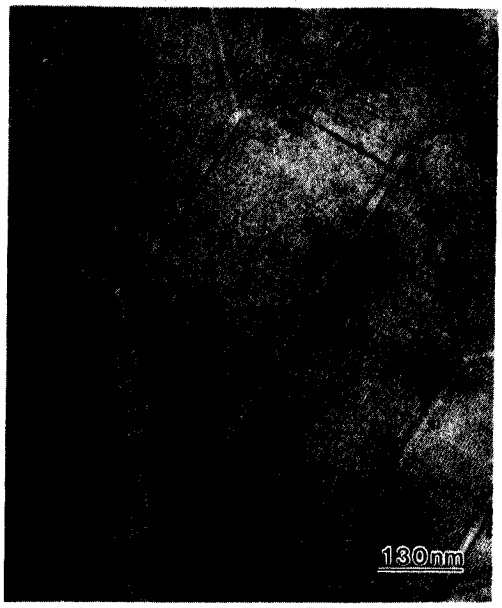

MONOCLINIC ZrO_2

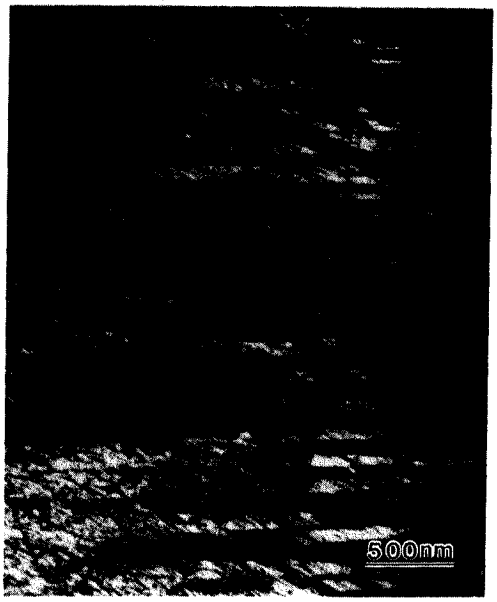

TETRAGONAL FeNi STEEL

Fig. 13

XBB 879-7500

Phase Shift for Antiphase Vectors in the DO_3 Phase

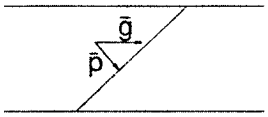

phase factor
$\alpha = 2\pi\bar{g}\cdot\bar{p}$

h k l	type of reflection	phase shift (α) 1/4<111>	phase shift (α) 1/2<100>	extinction distance (Å)
111	S	±π/2	±π	2,467
200	S	±π	0	2,498
220	F	0	0	272
311	S	±π/2	±π	2,752
222	S	±π	0	2,832
400	F	0	0	404

F : Fundamental reflection
S : Superlattice reflection

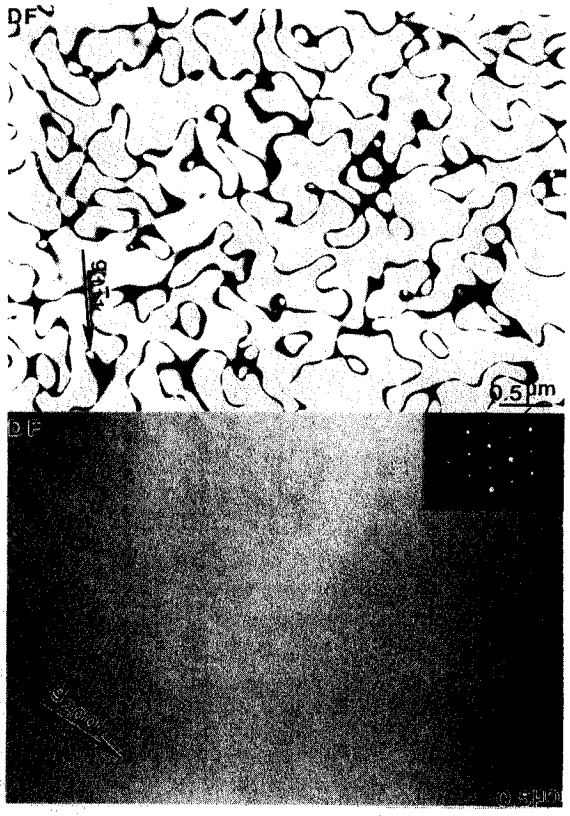

XBB 885-5242

Fig. 14

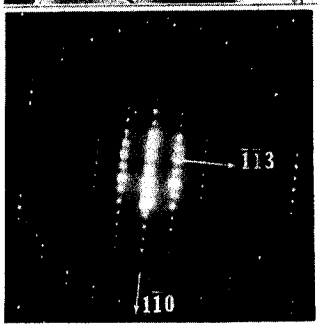

XBB 766-5394

Fig. 15

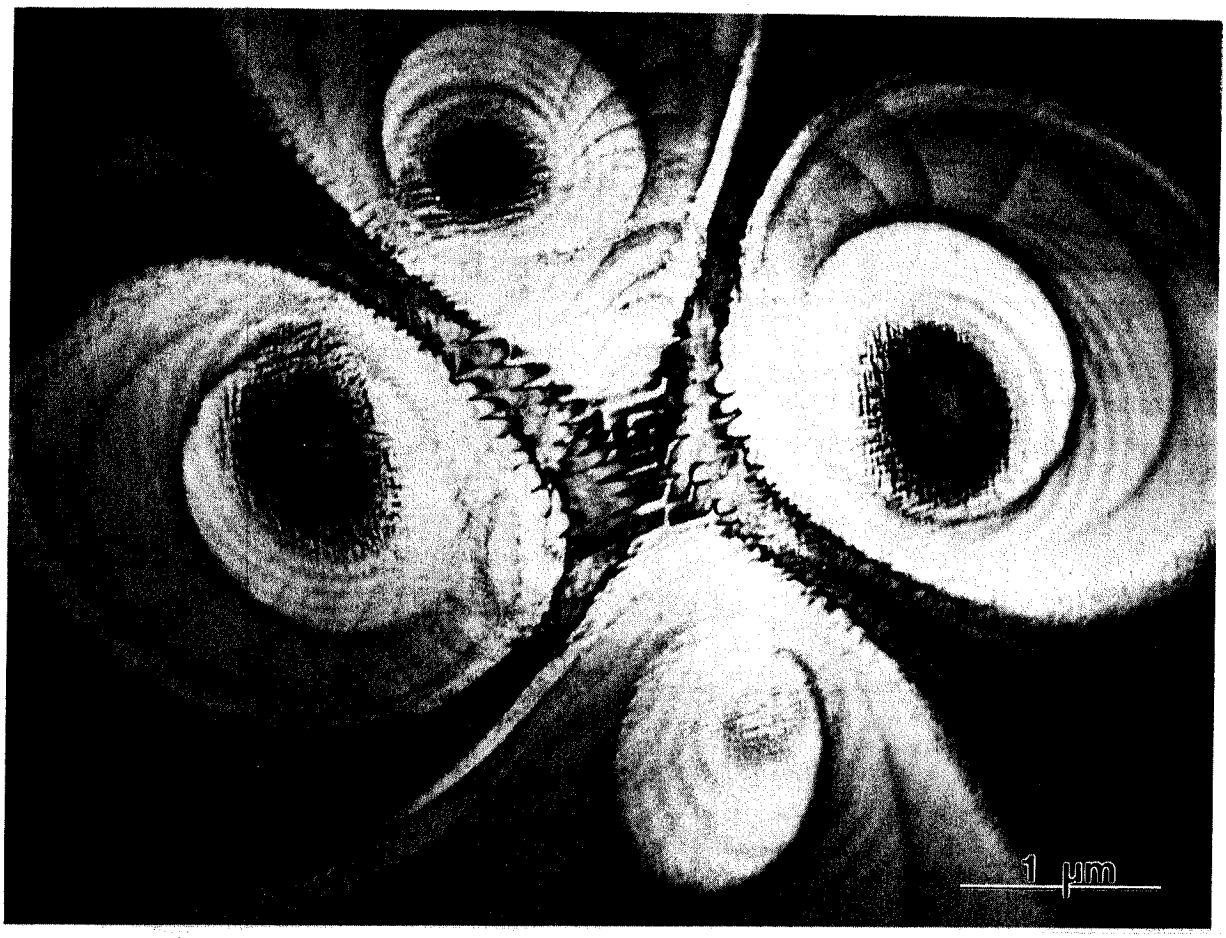

XBB 889-8927

Fig. 16

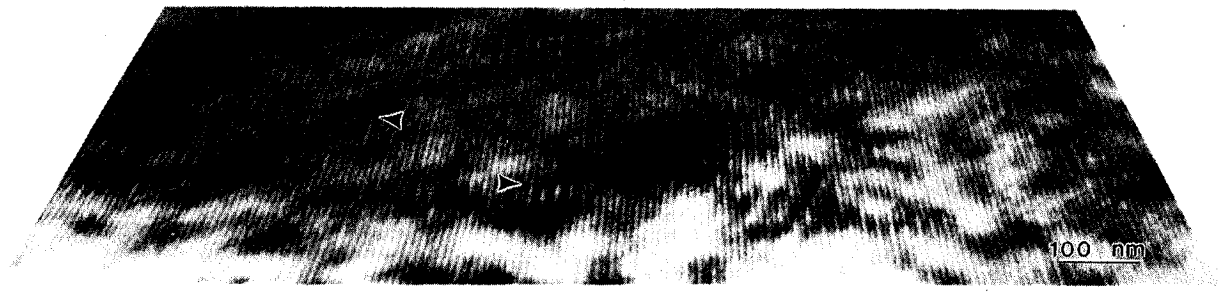

XBB 746-3669

Fig. 17

MAGNETIC DOMAINS AND DOMAIN WALLS IN COBALT

BACKGROUND - THE DOMAINS AND DOMAIN WALLS ARE REVEAL BY THE DEFLECTION THEY PRODUCE IN THE ELECTRON BEAM THE MICROSCOPE. IN COBALT THE WALLS ARE ABOUT 150 Å THI AND LIE PARALLEL TO {0001}, THE DIRECTION OF EASY MAGNI IZATION. THE WIDTH AND SHAPES OF THE OBSERVED DOMAIN IMAGES DEPEND ON THE PHYSICAL NATURE OF THE WALL AND ANGLE WHICH THE {0001} DIRECTION MAKES WITH THE PLANE C OBSERVATION.

DESCRIPTION OF THE OUT-OF-FOCUS METHOD - THE REVERSAL OF MAGNETIZATION DIRECTION CAUSES THE ELECTRON BEAM BE DEFLECTED IN OPPOSITE DIRECTIONS IN ADJOINING DOMAIN IF ONE FOCUSES ON THE IMAGE BELOW THE PLANE OF THE FOI (OVERFOCUSED IMAGE) THE DEFICIENCY OF ELECTRONS AT A AND THE EXCESS AT B PRODUCES BLACK AND WHITE LINES WH WIDTH IS PROPORTIONAL TO THE DEGREE OF DEFOCUSING. TI CONTRAST IS REVERSED (C AND D) IF A VIRTUAL IMAGE IS OB- SERVED BY FOCUSING ABOVE THE PLANE OF THE FOIL (UNDER- FOCUSED IMAGE).

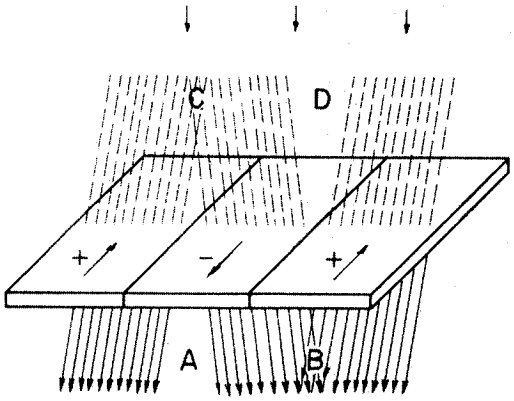

DOMAIN WALLS IMAGED BY THE OUT-OF-FOCUS METHOD - THE WALLS ARE BLACK AND WHITE LINES (A, B).

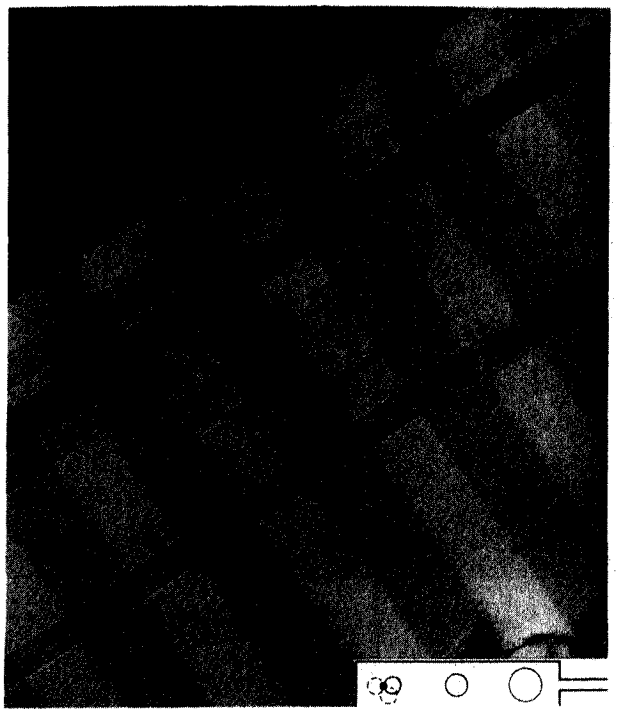

DOMAINS IMAGED BY THE MODIFIED DISPLACED APERTURE METHOD - THE TRANSMITTED BEAM IS NOT "VISIBLY" SPLIT, HOWEVER THE APERTURE POSITION IS MANIPULATED ABOUT THE SPOT, WHILE OBSERVING THE IMAGE, UNTIL THE DOMAINS, A, APPEAR. THIS METHOD EMPLOYS A SPECIMEN HOLDER WITH HIGH RESOLUTION PLUS DOUBLE TILTING FOR MAXIMUM CON- TRAST. NOTE ALSO THE FAULTS, B, and DISLOCATIONS, C.

DOMAINS IMAGED BY THE DISPLACED APERTURE METHOD - THE OBJECTIVE APERTURE IN THE BACK FOCAL PLANE IS POSITIONED SO THAT IT STOPS OUT ONE OF THE DIVIDED BEAMS. ALTERNATE DOMAINS (A, B) APPEAR BLACK AND WHITE. A LONG FOCAL LENGTH HOLDER IS NECESSARY TO SPLIT THE SPOTS.

Fig. 18

XBB 879-7485

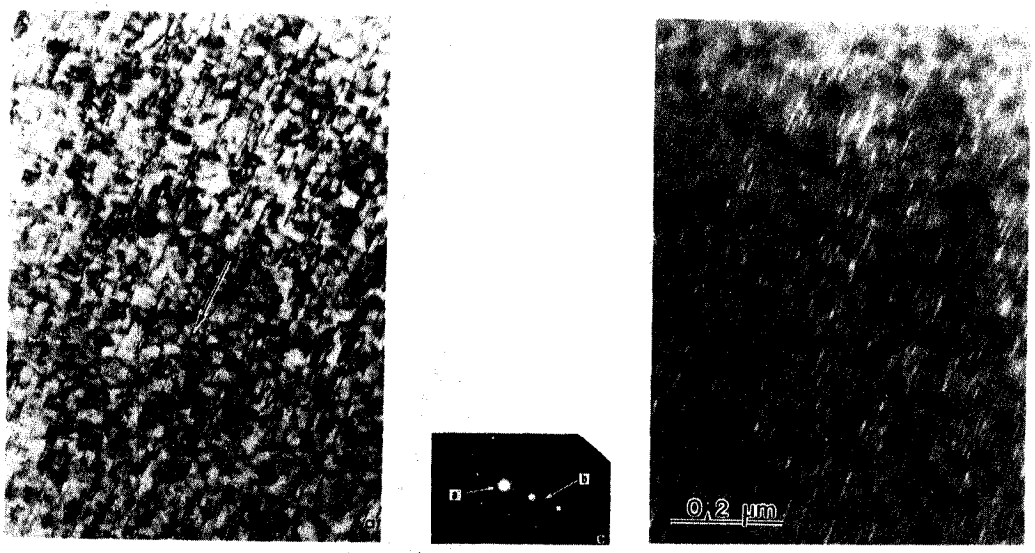

XBB 699-6018

Fig. 19

XBB 695-3420A

Fig. 20

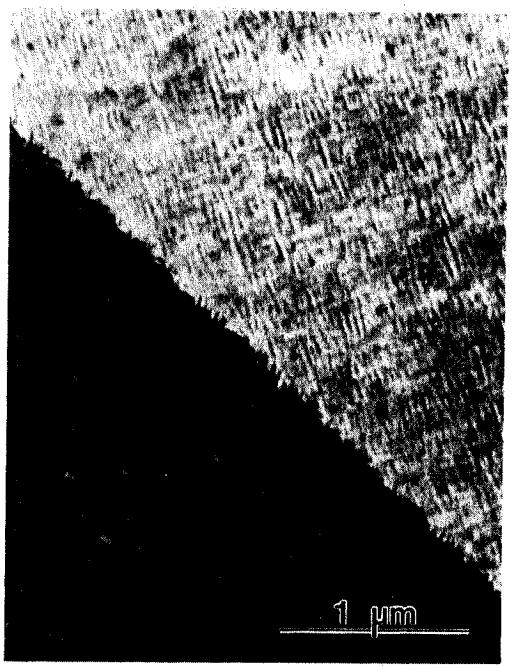

XBB 695-3420A

Fig. 21

Decomposition initially follows a coarsening law $\bar{\lambda} = kt^{1/3}$ with copper-rich and copper-poor regions growing at approximately constant volume fraction and compositional amplitude. At wavelengths exceeding ~1000Å interface dislocations are created and the coarsening rate is accelerated.

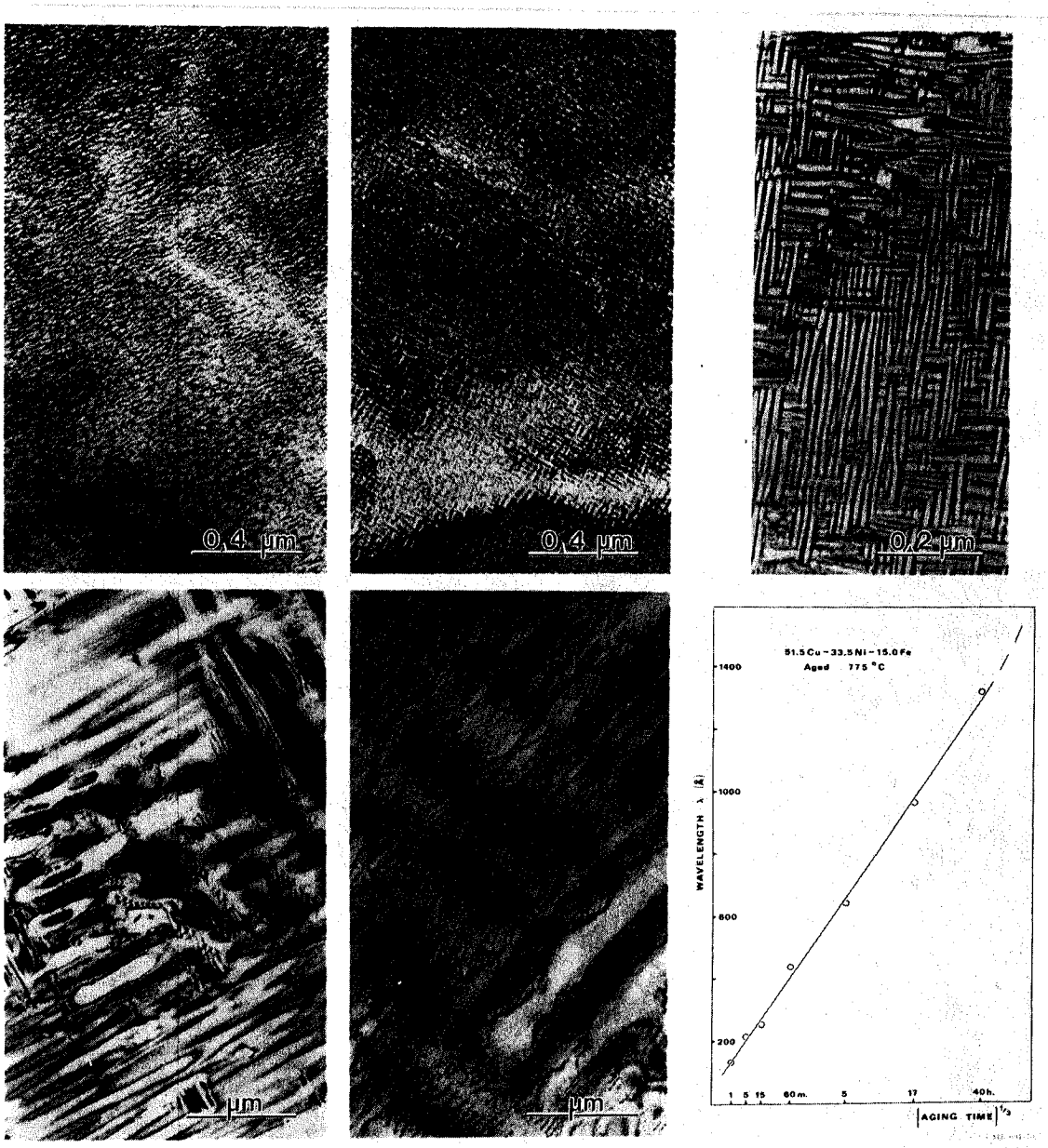

XBB 889-8930

Fig. 22

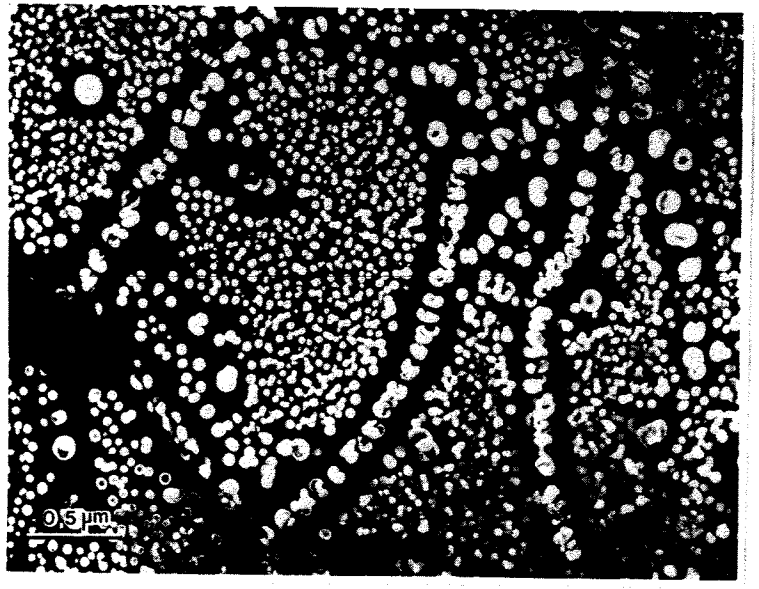

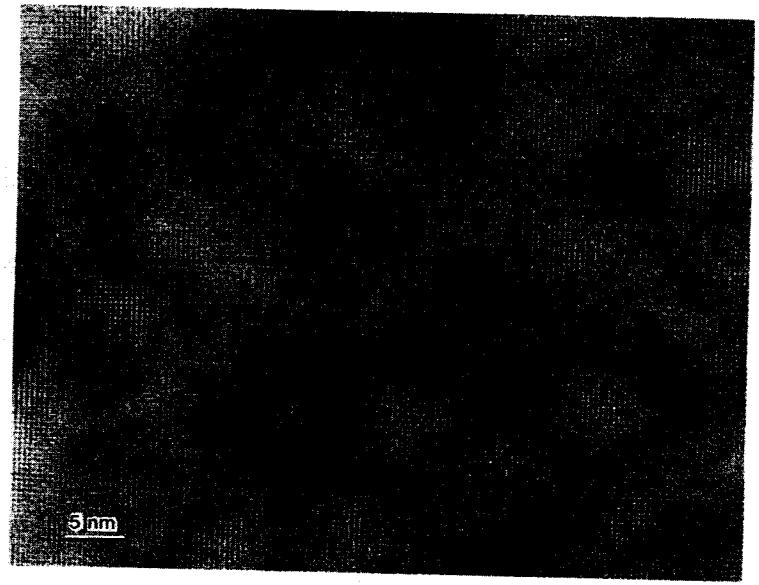

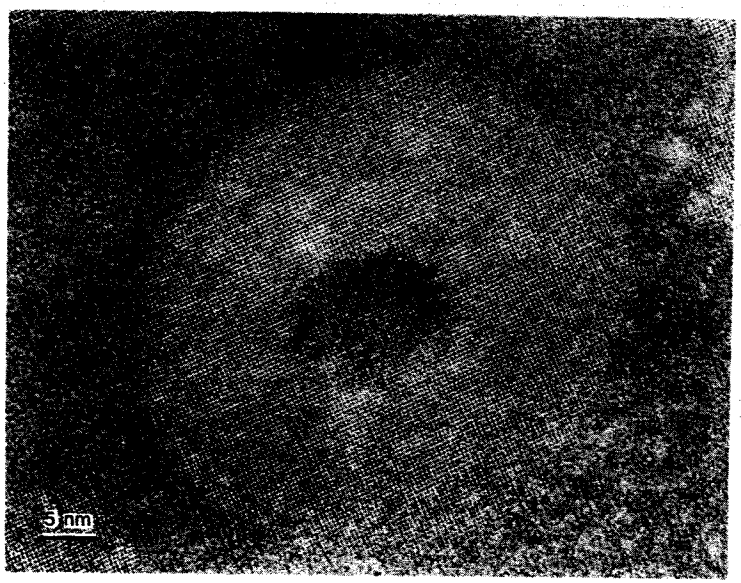

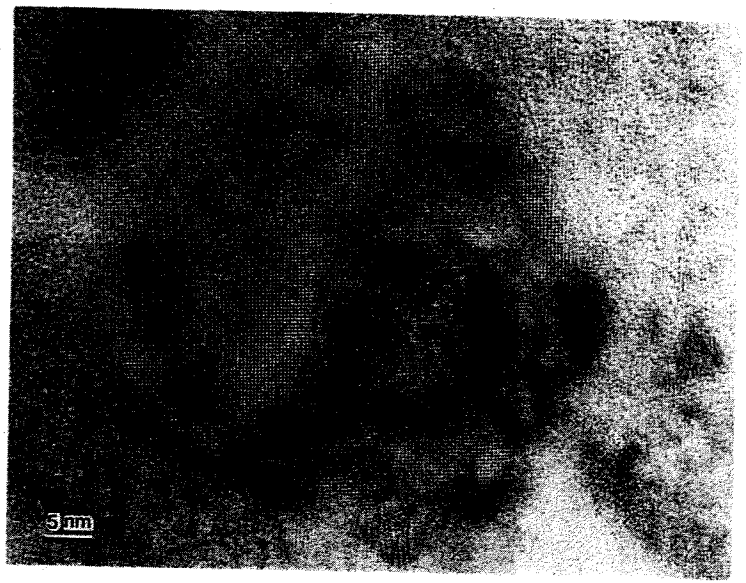

Fig. 23 (above)
Fig. 25 (below)

Fig. 24 (above)
Fig. 26 (below)

XBB 889-9130

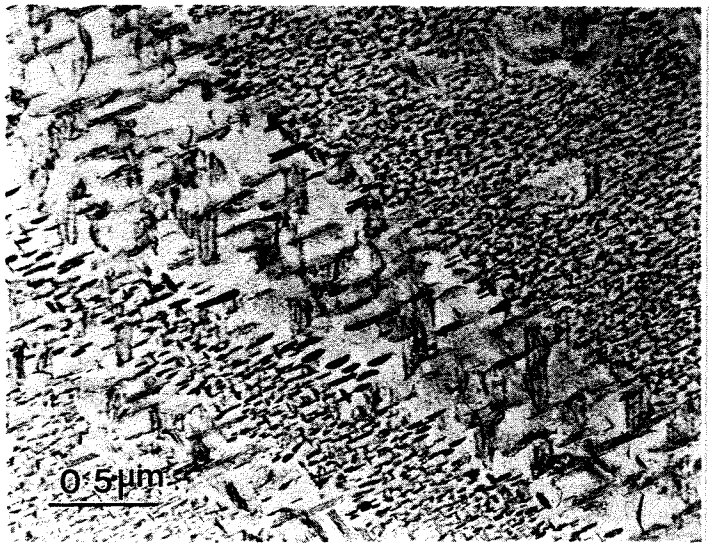

Fig. 27

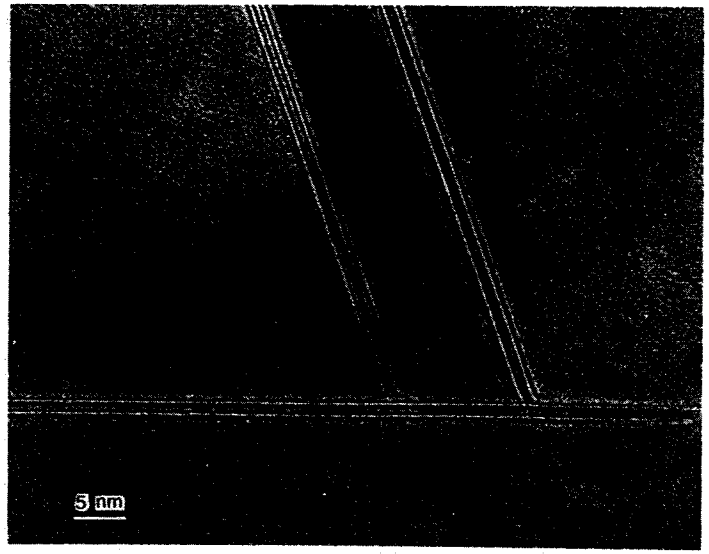

Fig. 28

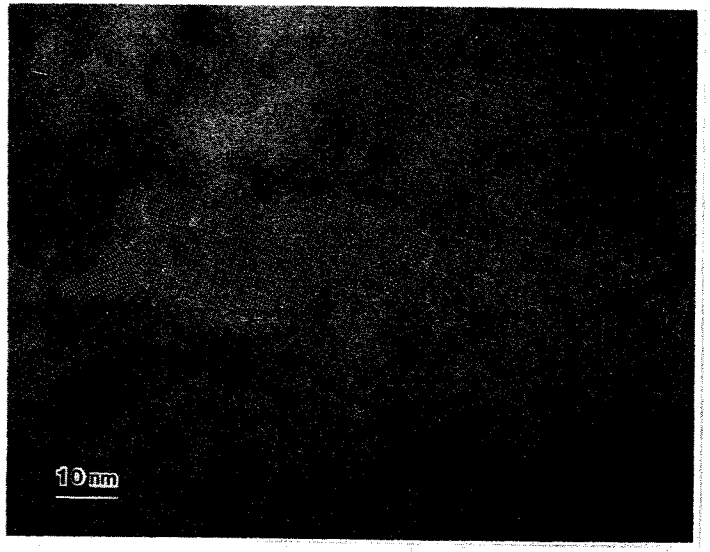

Fig. 29

Fig. 30

XBB 8810-9732

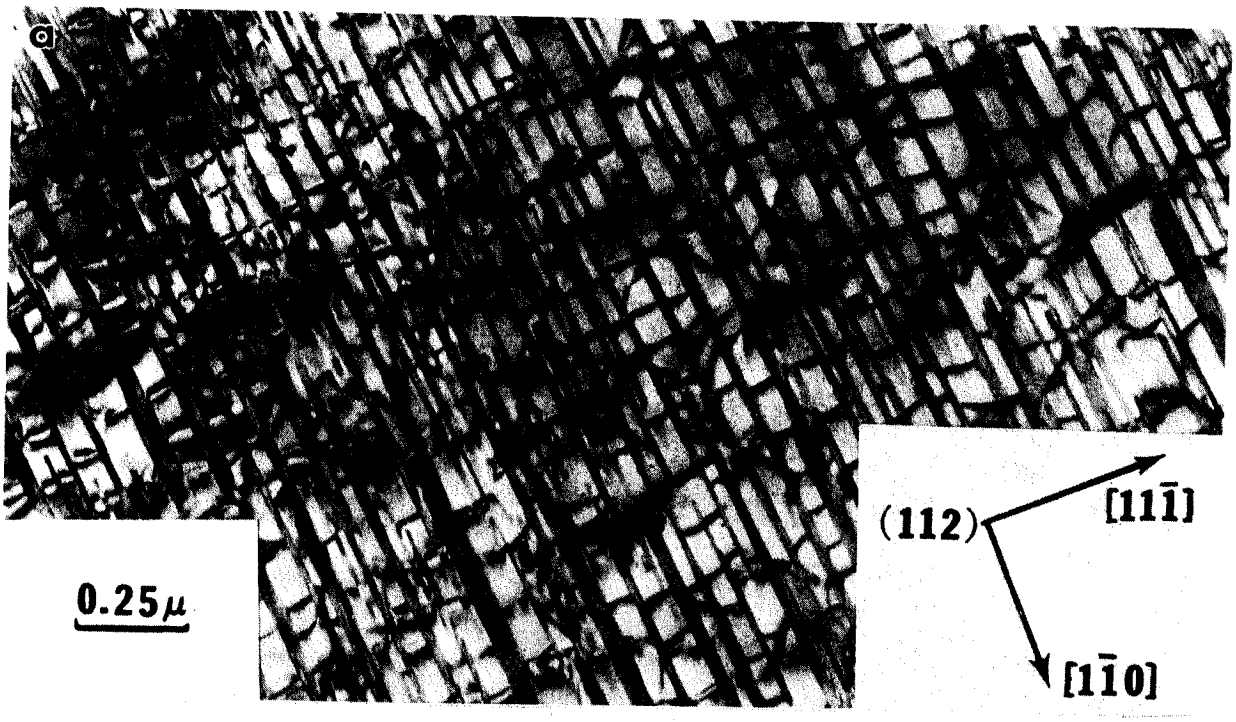

IM 2160

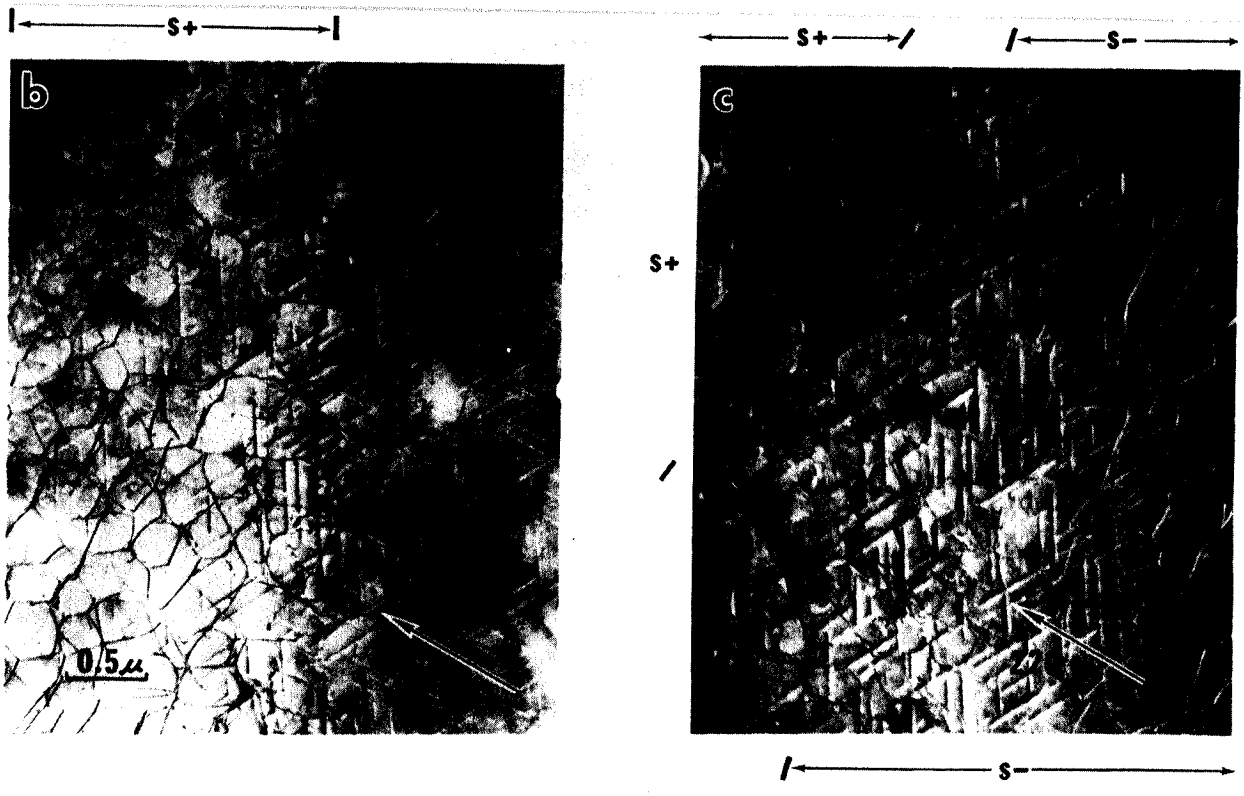

IM 2165

Fig. 31

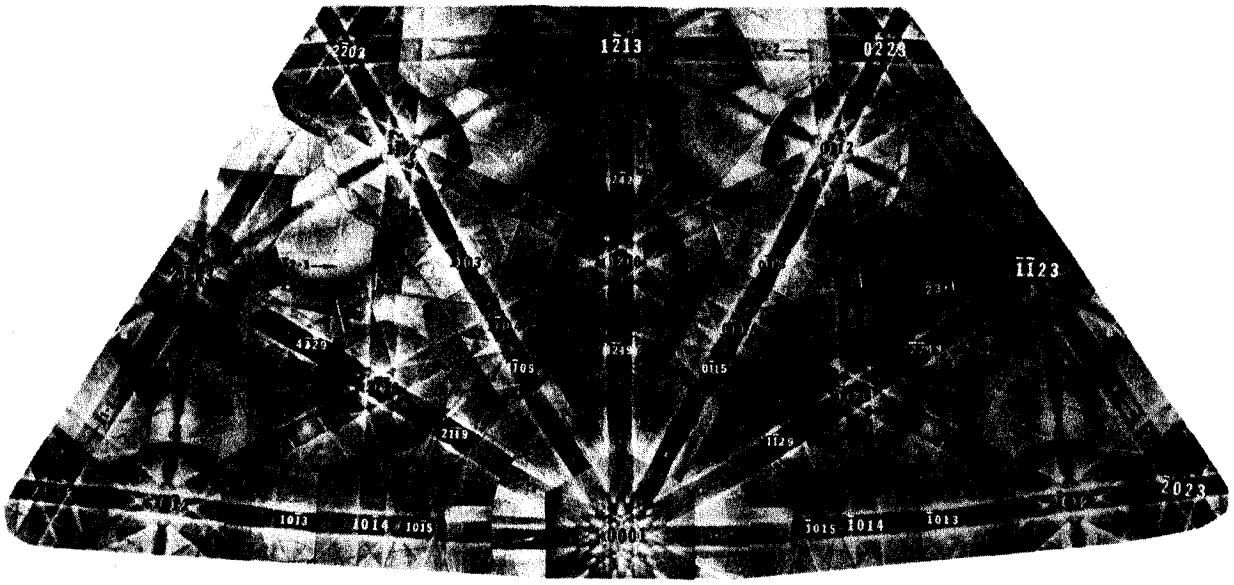

Fig. 32 IM 2160

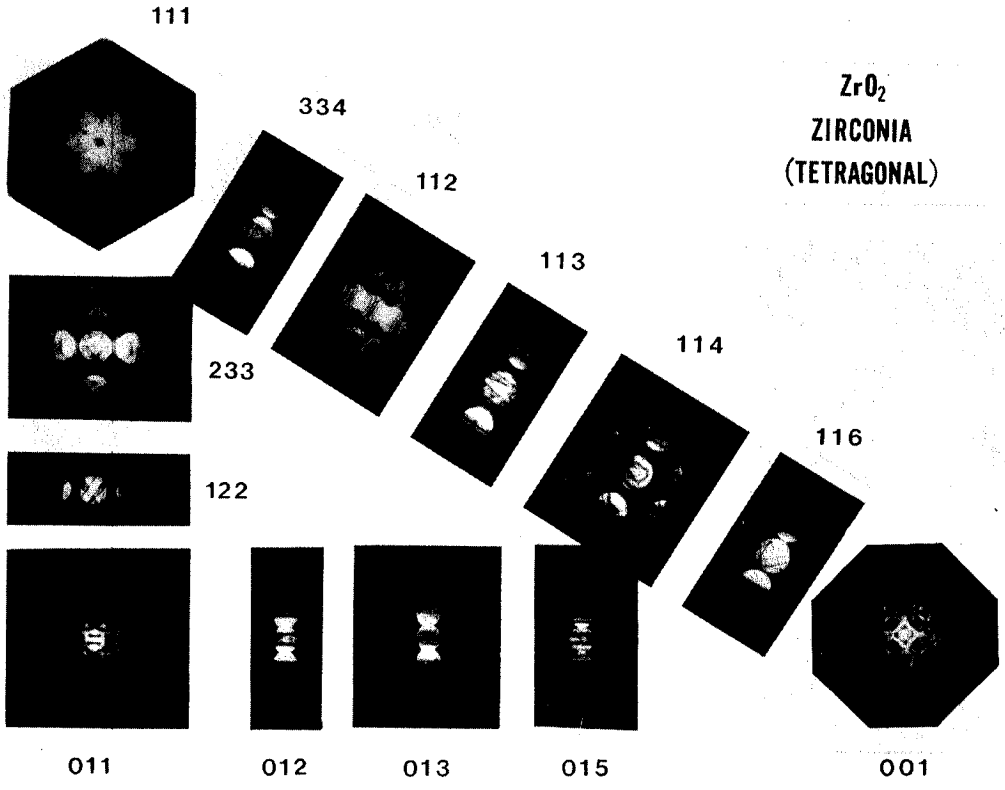

XBB 866-5362

Fig. 33

CARBON PARTITIONING IN RETAINED-AUSTENITE IN LATH-MARTENSITIC STEELS

TRANSMISSION ELECTRON MICROSCOPE - IMAGE STUDIES

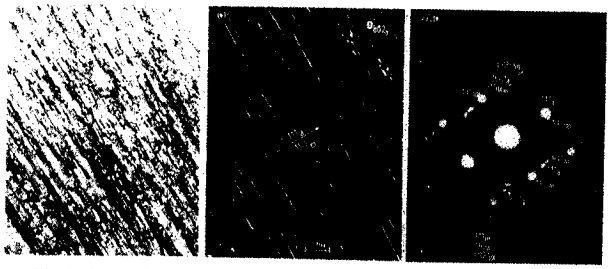

FIGURE 1 - (a) BF and (b) DF ($\bar{1}11$)$_\gamma$ images illustrating the general appearance of thin films of Ret-γ at the martensite lath boundaries (0.5 at.% C steel). (c) Composite SAD pattern of martensite (α) and austenite (γ).

The microstructure consists of dislocated lath martensite with fairly straight boundaries and thin film Ret-γ at the lath-like martensite crystal boundaries. DF micrographs (fig. 1) show an extensive amount of Ret-γ (5 vol.%) even at this low carbon level. The existence of this high temperature phase at low temperatures is attributed to several mechanisms in which interstitial C stabilizes the austenite. (i) Chemical stabilization: Diffusion and partitioning of C in Ret-γ decrease the local M_s temperature and inhibit further transformation. (ii) Thermal stabilization: During quenching interstitial C forms dislocation atmospheres in α' and at the α'/γ interface, pinning the dislocations and suppressing interface motion. (iii) Mechanical stabilization: Part of the austenite to martensite shear transformation strains is accommodated by soft γ which deforms extensively to prohibit the transformation.

The average C concentration in Ret-γ can be determined by measurements of shift in positions of the ndiz lines in CBED patterns in relation to the change in the lattice parameter of the Ret-γ, due to C: $(\Delta a/a_{ref}) = (2/3)[(p_i/q_i)^2 - (p_{ref}/q_{ref})^2](\delta/115)^2$. Ni (99.99% with $a_o = 3.5238$) was used as a reference, and results cross-checked with Cu (99.999% with $a_o = 3.6150$). For the example shown in fig. 2, C at.% = 4.9 - 0.6 (at.% C alloy - 0.7) taking $a_{Ret-\gamma} = 3.555 + 0.044X$ (w/o C).

Retained austenite (Ret-γ) has been identified in a number of carbon containing lath martensitic steels with M_s and M_f temperatures well above room temperature. Because of its beneficial effects on the mechanical properties (especially fracture toughness) of HSLA steels the influence of interstitial C in stabilizing the γ has been studied in detail using TEM, CBED and FIM-APA techniques.

Steels were austenitized at 1100°C, and oil quenched. TEM foils were prepared by electropolishing in chromacetic at room temperature (RT), and Cu and Ni standards in 25% NHO_3 in CH_3-OH at -30°C. Some steel foils were etched for CBED by "dipping" in 15% $HClO_4$-5% $C_3H_5(OH)_3$-CH_3COOH at -25°C. FIM tips were electropolished in 25% $HClO_4$ in CH_3-COOH at RT.

CONVERGENT BEAM ELECTRON DIFFRACTION

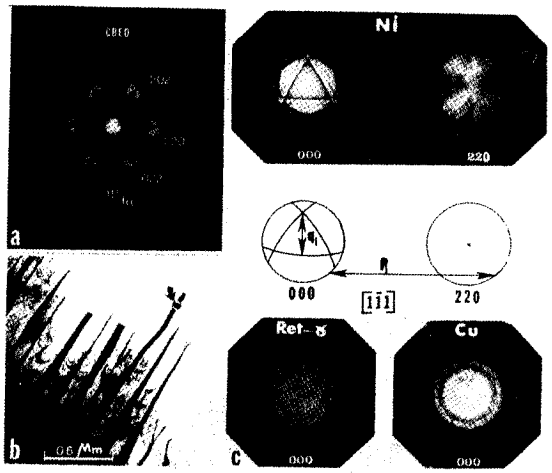

FIGURE 2 - (a) Nickel (fcc) [ii] CBED-pattern at 100 kV reveals trigonal symmetry. (b) BF image, from a specially prepared foil, shows the Ret-γ films extending into the perforation. (c) Discs formed by forward scattered beams from Ni, Ret-γ, and Cu (note q_i and p_{ij}).

FIELD ION MICROSCOPY - ATOM PROBE ANALYSIS

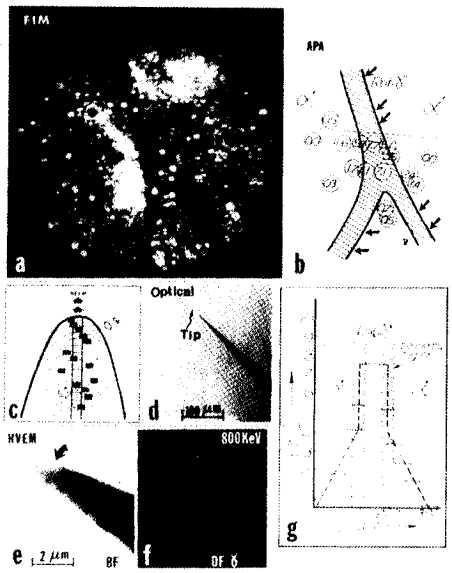

Atom probe analysis provided direct quantitative determination of the C distribution in α' and Ret-γ at 20-30 Å resolution. Considerable C enrichment occurs in Ret-γ - direct evidence of chemical stabilization (figs. 3-4). Detailed measurements of C distribution in a thicker Ret-γ film (fig. 4) gave an average concentration of 3.0 at.% and up to 8.5 at.% at the α'/Ret-γ interface (Thermal stabilization). The extent of deformation (Mechanical stabilization) is discernible in TEM micrographs in fig. 4. There is no apparent change in distribution of substitutional alloying elements (Cr and Mn, fig. 4) in α' and Ret-γ. Hence changes in the amount of Ret-γ with alloying elements are attributed to their interaction with C influencing its mobility. Thus the overall stability of thin film Ret-γ is due to effects of several mechanisms.

FIGURE 3 - (a) FIM image of Ret-γ. (b) Regions of APA analysis. (c) Illustration of the analysis of subsurface regions by field evaporation. (d) Low magnification image of the tip. (e) HVEM BF and (f) DF images reveal Ret-γ. (g) Concentration profile for C across the interface.

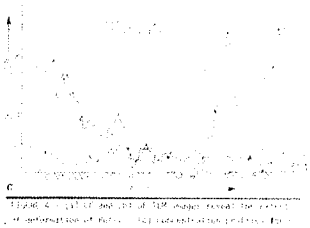

FIGURE 4 - (a) BF and (b) DF TEM images reveal the extent of deformation of Ret-γ. (c) Concentration profiles for C and Mn across the α'/Ret-γ interface (APA).

XBB 817-7029

Fig. 34

INVESTIGATION OF MOON DUST FROM APOLLO 11

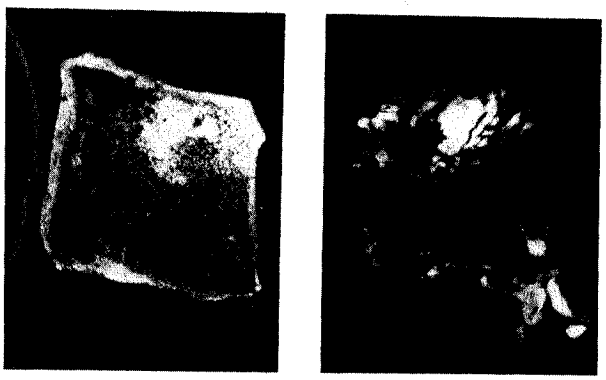

Flakes of mineral showing radiation damage and heavy ion tracks.

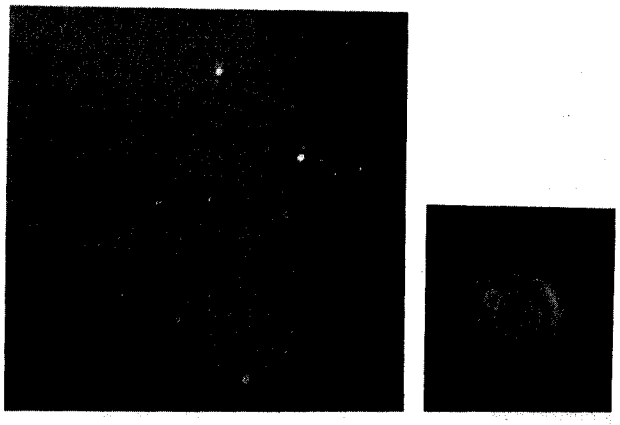

Identification of very small particles of α-Fe in amorphous matrix.

XBB 879-7482

Fig. 35

Glassy intergranular phase R and an inclusion S at a triple grain junction of $Ba_2(Cu,Zn)$-ferrite.

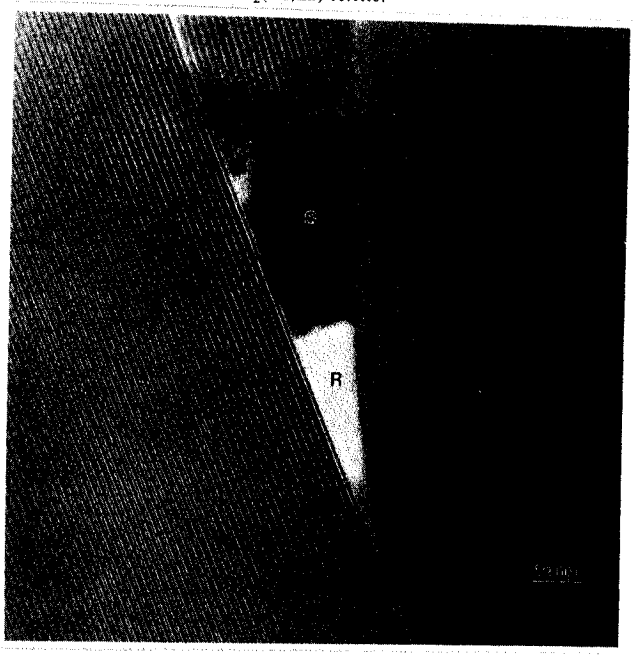

XBB 888-8421

Fig. 36

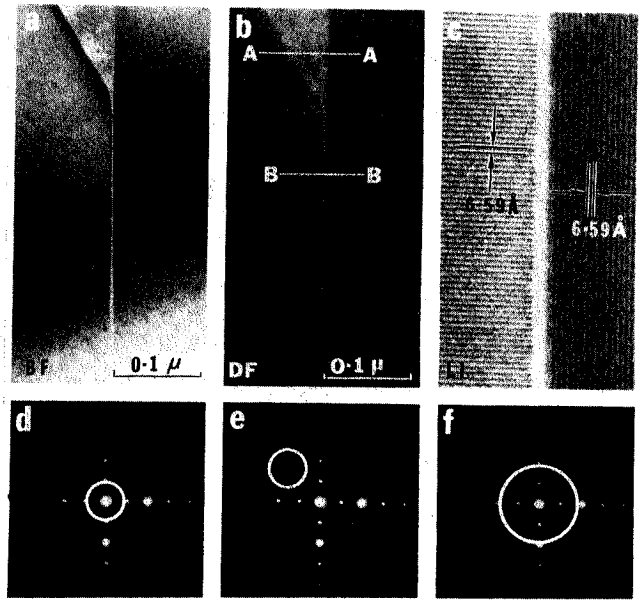

XBB 787-8787

Fig. 37

XBB 854-2600

Fig. 38

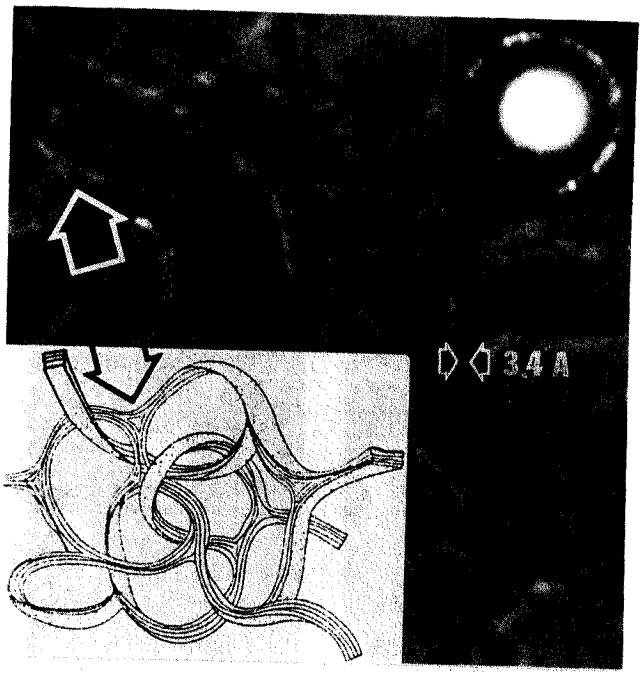

XBB 785-6028

Fig. 39

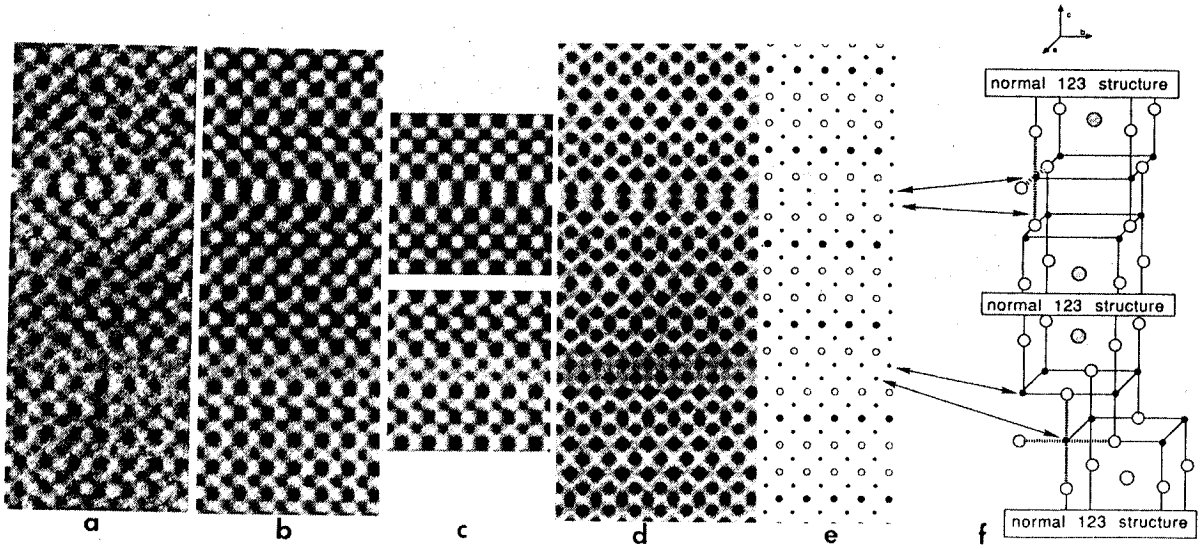

XBL 8711-4634

Fig. 40

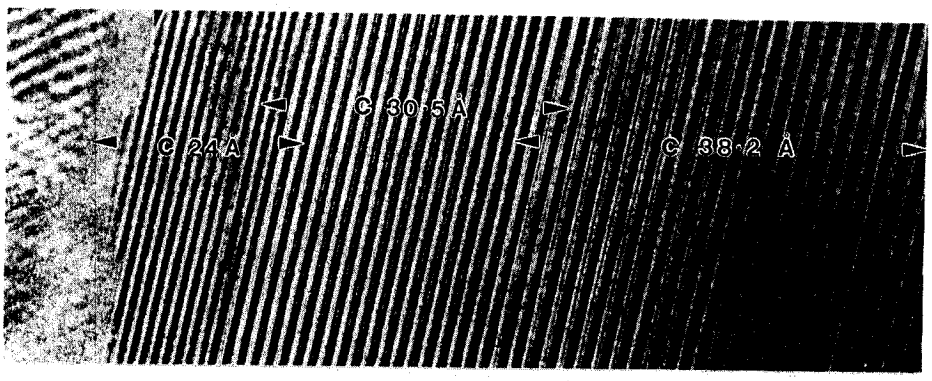

XBB 885-4701

Fig. 41

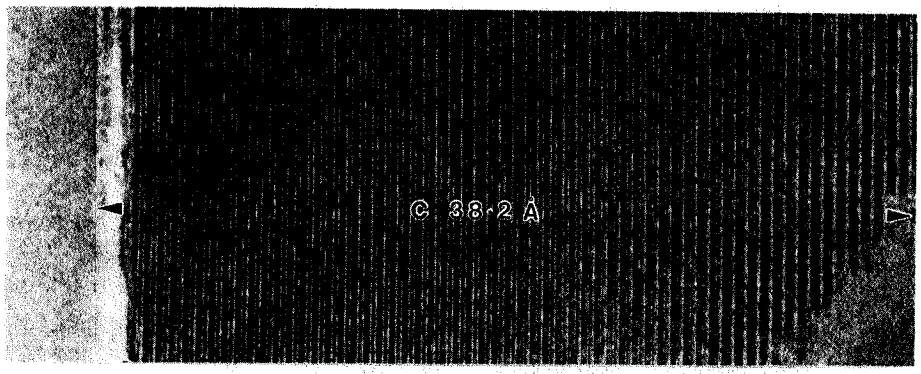

XBB 888-8385

Fig. 42

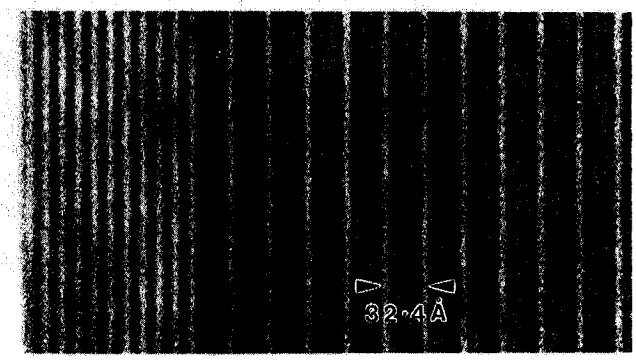

XBB 889-8746

Fig. 43

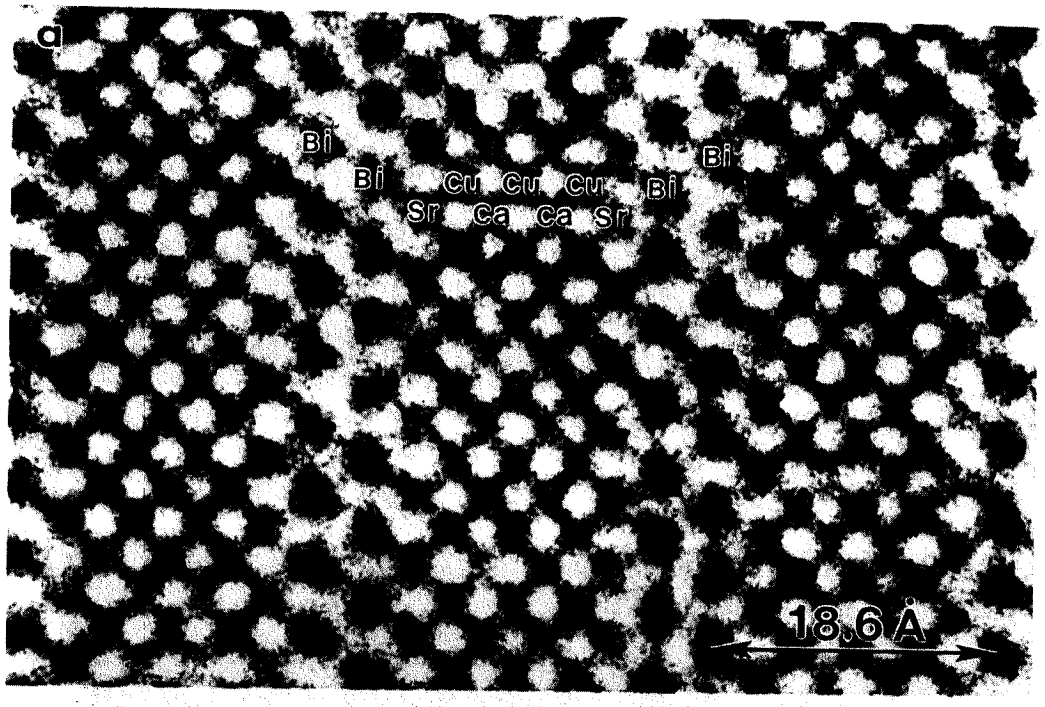

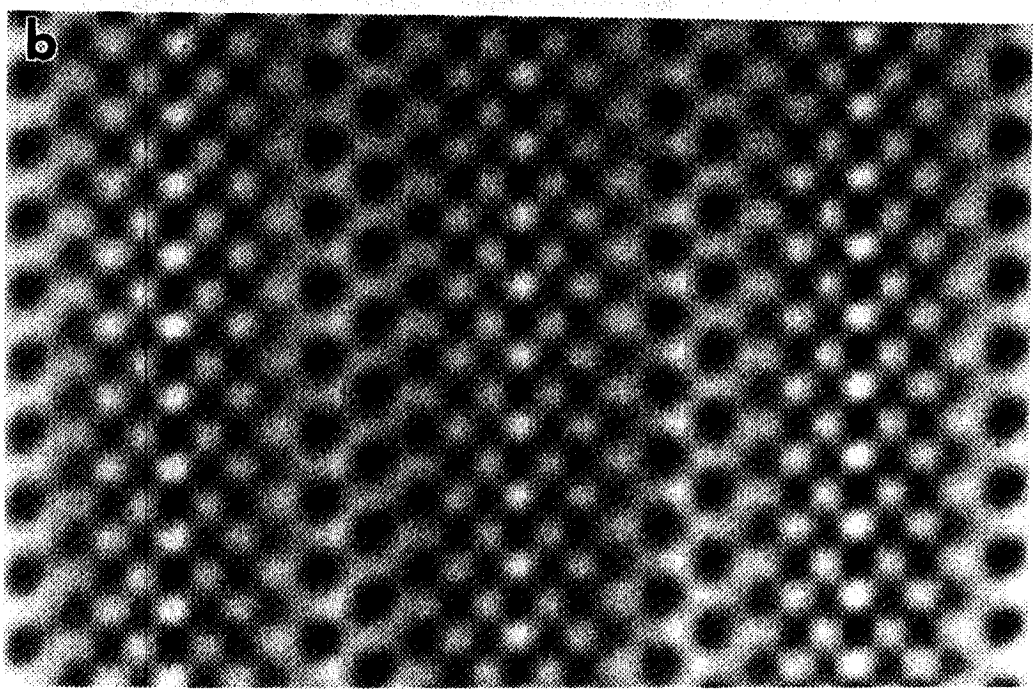

$Bi_2Sr_2Ca_2Cu_3O_y$ (2-2-2-3) T_c = 110K c=37.2Å

Fig. 44

XBB 885-4984A